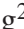


## Original article

# A noise-resistant and annotation-free supervoxel-based algorithm for rapid segmentation of multiphase X-ray images

Shanlin Ye<sup>1,3</sup>, Xianzhi Song<sup>2</sup><sup>\*</sup>, Zhuangzhuang Ma<sup>1</sup>, Yang Gao<sup>3</sup>, Linqi Zhu<sup>1</sup>, Mengmeng Zhou<sup>2</sup>, Lizhi Xiao<sup>3</sup>, Gege Wen<sup>1</sup>, Branko Bijeljic<sup>1</sup>, Martin J. Blunt<sup>1</sup>

<sup>1</sup>Department of Earth Science and Engineering, Imperial College London, London SW7 2BP, United Kingdom

<sup>2</sup>State Key Laboratory of Petroleum Resources and Prospecting, China University of Petroleum, Beijing 102249, P. R. China

<sup>3</sup>College of Artificial Intelligence, China University of Petroleum, Beijing 102249, P. R. China.

### Keywords:

X-ray images  
image processing  
supervoxel segmentation  
curvature  
contact angles

### Cited as:

Ye, S., Song, X., Ma, Z., Gao, Y., Zhu, L., Zhou, M., Xiao, L., Wen, G., Bijeljic, B., Blunt, M. J. A noise-resistant and annotation-free supervoxel-based algorithm for rapid segmentation of multiphase X-ray images. *Advances in Geo-Energy Research*, 2025, 16(1): 50-59.  
<https://doi.org/10.46690/ager.2025.04.06>

### Abstract:

This study introduces a three-dimensional supervoxel segmentation method to accurately separate solid and fluid phases in X-ray images of porous materials, with applications in energy research. Compared with intelligent segmentation algorithms requiring model training, the proposed method operates as a ready-to-use solution with significantly enhanced efficiency. When benchmarked against conventional approaches such as watershed transformation, our technique demonstrates superior segmentation accuracy. Tested on porous rock and gas diffusion layers under varying wettability, it accurately quantifies fluid saturation, interfacial area, curvature, and contact angles—key parameters for enhanced oil recovery, CO<sub>2</sub> storage, and hydrogen fuel cells. The proposed three-dimensional segmentation method is noise-resistant and annotation-free, improving both the accuracy and efficiency of segmenting diverse micro-structural material datasets and providing reliable measurements of their geometric characteristics.

## 1. Introduction

The X-ray Micro-computed tomography (micro-CT) has gained widespread application in recent years in fields such as materials science and energy research (Blunt et al., 2013; Liu et al., 2023; Zhao and Lu, 2023). This technique offers non-destructive, high-resolution Three-dimensional (3D) images that reveal the internal micro-structure of materials, including the distribution of fluids in the pore space (Schlüter et al., 2014; Zeng et al., 2022; Zhu et al., 2022; Isah et al., 2024). Such insights are invaluable for applications like evaluating the efficiency of CO<sub>2</sub> sequestration, optimizing hydrocarbon recovery from porous rocks (Yang et al., 2021; Yang et al., 2023).

Micro-CT records local X-ray adsorption, resulting in gray-

scale images: for further analysis it is necessary to segment this image to identify mineral and fluid phases (Wildenschild and Sheppard, 2013).

However, due to the complexity of porous material structures, achieving accurate segmentation is highly challenging. Currently, three types of method are widely employed. (1) Traditional methods, such as watershed segmentation, use gray-scale and gradient information to identify phases. These algorithms do not require pre-labeled training data and can provide highly accurate boundary lines, which has led to their widespread use (Andrew et al., 2014; Reynolds et al., 2017). However, the results are sensitive to noise, typically requiring filtering techniques and manual intervention to improve and optimize performance. (2) Another approach is to apply a machine learning method where the user manually labels

phases on the image for training. Weka segmentation is an example of this approach that can achieve good results, but relies on the quality of the user-based training (Alhammedi et al., 2017; Arganda-Carreras et al., 2017; Ibekwe et al., 2020; Garfi et al., 2020). (3) With advances in deep learning, neural network-based segmentation methods such as U-Net (Mahdaviara et al., 2023b; Siavashi et al., 2024) and SegNet (Da Wang et al., 2021) have been applied to 3D images of porous materials. These models can offer higher accuracy compared to watershed and Weka segmentation. However, training neural networks requires large amounts of high-quality labeled data, which is a time-consuming process. Consequently, many segmentation models are trained not on manually labeled data but on segmentation results obtained from watershed and Weka, resulting in sub-optimal performance (Liang et al., 2022; Li et al., 2023; Mahdaviara et al., 2023a; Siavashi et al., 2024). Furthermore, deep learning models often exhibit unstable transfer ability, making it difficult to develop a model that can be applied to various porous media images without an extensive training dataset. Even a general image segmentation model, such as the segment anything model (Kirillov et al., 2023), has been shown to underperform in porous media segmentation tasks. While some researchers have attempted to build segmentation models using unsupervised neural network training methods (Mahdaviara et al., 2023a), achieving precise segmentation results still requires post-processing techniques. Another limitation of deep learning models is that, due to hardware constraints, most training images are either manually cropped two-dimensional (2D) images (Siavashi et al., 2024) or very small 3D samples (Da Wang et al., 2021; Mahdaviara et al., 2023b; Zhu et al., 2024), limiting their ability to capture 3D information particularly if there is long-range spatial correlation.

In summary, although various segmentation methods exist for the task of segmenting 3D images of porous media, traditional methods perform poorly on low-quality images which need filtering techniques and manual intervention. Machine learning and deep learning methods, meanwhile, often depend on large, high-quality, already labeled datasets, with training requiring substantial computational resources and time. Basically, you need to segment an image already to train a deep learning model to reproduce what you already know. Additionally, the limited transfer ability of machine learning models restricts their applicability across different materials and imaging conditions.

This work proposes a segmentation method that does not require labeled data, and demonstrates superior accuracy compared to conventional methodologies such as watershed, which is an extension of superpixel segmentation into 3D. Superpixel segmentation is a widely-applied image segmentation method that groups pixels into similar regions, known as superpixels (Vincent and Soille, 1991; Vedaldi and Soatto, 2008; Achanta et al., 2012; Stutz et al., 2018). This technique effectively reduces noise and redundant information in the image while preserving edge and structural information, enabling rapid and accurate segmentation. Through validation for different porous materials and under various experimental conditions, the proposed segmentation method is shown to significantly improve

both efficiency and accuracy, particularly for complex, noisy datasets. Compared with intelligent segmentation algorithms requiring model training, the proposed method operates as a ready-to-use solution with significantly enhanced computational efficiency. When benchmarked against conventional approaches such as watershed transformation, our technique demonstrates superior segmentation accuracy. Furthermore, the algorithm exhibits notable adaptability to raw, unfiltered image data. This innovative approach provides a new direction for the further development of imaging and digital rock technology, with broad potential applications in porous media research.

## 2. Materials and methods

### 2.1 Rock samples for segmentation

To verify the general applicability of our proposed segmentation method, this work collected X-ray images of various porous media with most of them available on the open-source platform Digital Rocks Portal ([www.digitalrocksportal.org](http://www.digitalrocksportal.org)). Eight 3D images were considered: example 2D cross sections are shown in Fig. 1.

- 1) A filtered image of Bentheimer sandstone with a voxel size of  $3.58 \mu\text{m}$  acquired using a Zeiss Versa 510 X-ray microscope under water-wet conditions. The pore space contains two fluid phases: oil and brine imaged during brine injection at a fractional flow of 0.5 (Lin et al., 2018).
- 2) Similar to image 1 but under mixed-wet conditions (Lin et al., 2019).
- 3) An unfiltered version of image 2.
- 4) A lower resolution image of Bentheimer sandstone with oil and water in the pore space (voxel size of  $7.0 \mu\text{m}$ ) (Ramstad et al., 2012).
- 5) A filtered image of a reservoir carbonate from the Middle East with a voxel size of  $2.0 \mu\text{m}$  acquired using a Zeiss Versa 510 X-ray microscope under weakly water-wet conditions. Again the pore space contains oil and brine (Alhammedi et al., 2017).
- 6) Similar to image 5 but under mixed-wet conditions.
- 7) An filtered image of Ketton limestone with a voxel size of  $2.0 \mu\text{m}$  with oil and water in the pore space (Yang and Zhou, 2020).
- 8) An image of a gas diffusion layer with a voxel size of  $2.05 \mu\text{m}$ . The material contains 40% polytetrafluoroethylene coating. Air and water occupy the pore space. The solid phase in this sample is fibrous, differing from conventional rock structures (Shojaei et al., 2022).

### 2.2 Supervoxel segmentation algorithm

This study propose a noise-resistant and annotation-free supervoxel-based algorithm designed for efficient and accurate 3D X-ray images segmentation. This algorithm represents an improvement over the 2D quickshift superpixel algorithm, which demonstrates superior edge detection capabilities compared to other superpixel algorithms, as shown in the Supplementary Information (Fig. S1).

The supervoxel-based segmentation algorithm clusters vox-

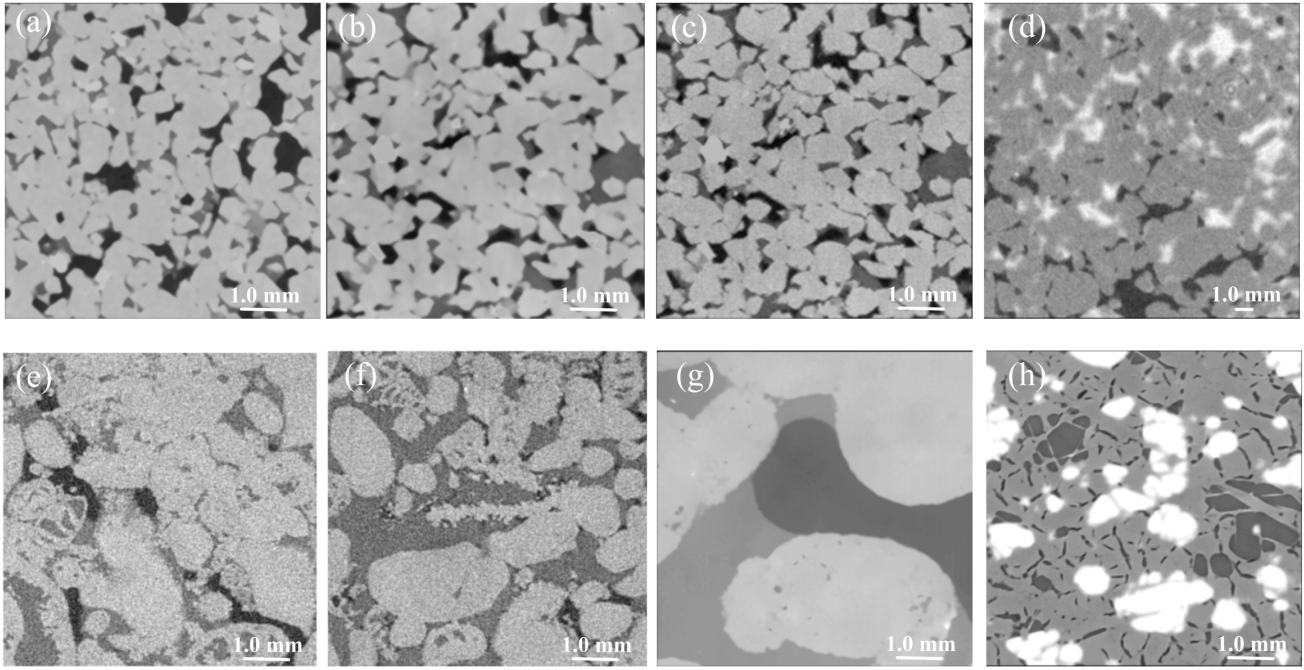


**Fig. 1.** Two-dimensional slices of the three-dimensional raw X-ray images considered in this work showing the normalized gray-scale intensity. (a,b) Images 1 and 2: Bentheimer sandstone with oil and water in the pore space under water-wet and mixed-wet conditions respectively. (c) Image 3: an unfiltered version of image 2. (d) Image 4: a lower resolution image of Bentheimer sandstone with oil and water in the pore space. (e,f) Images 5 and 6: a reservoir Middle East carbonate with oil and water in the pore space under weakly water-wet and mixed-wet conditions respectively. (g) Image 7: Ketton limestone with oil and water in the pore space. (h) Image 8: gas diffusion layer with air and water in the pore space.

els with high similarity into supervoxels, achieving better results in 3D data compared to superpixels formed from 2D data, as shown in the Fig. 2. The superpixel methods can only generate superpixels along a single plane ( $x$ - $y$ ), leading to poor segmentation performance in the other planes ( $x$ - $z$ ,  $y$ - $z$ ) upon completion.

The algorithm comprises the following key steps, which are detailed below and illustrated in Fig. 3.

### 2.2.1 Density estimation

The first step is to define a normalized gray-scale intensity  $I$ :  $0 \leq I \leq 1$ . It ensures that the image has voxels spanning the whole range from 0 to 1. Then to define a difference between two voxels  $p$  and  $q$ :

$$d_I^2(p, q) = [I(p) - I(q)]^2 \quad (1)$$

It also defines a physical distance:

$$d_S^2(p, q) = (x_p - x_q)^2 + (y_p - y_q)^2 + (z_p - z_q)^2 \quad (2)$$

where  $(x, y, z)$  is the coordinate of a center of a voxel with each voxel assumed to be a unit cube.

Then define a similarity between voxels  $p$  and  $q$ :

$$S(p, q) = d_S^2(p, q) + \alpha d_I^2(p, q) \quad (3)$$

where the parameter  $\alpha$  weights the gray-scale and spatial distances, set to  $\alpha = 10$  in this work.

Finally it defines a density representing overall the simi-

ilarity of voxels in the neighborhood  $N(p)$  of  $q$ :

$$D(p) = \sum_{q \in N(p)} \exp \left[ -\frac{S(p, q)}{2k^2} \right] \quad (4)$$

where  $N(p)$  denotes the set of neighboring voxels around  $p$ , with radius  $k$ . In this work takes  $k = 1$ , hence  $N(p)$  includes 26 neighboring voxels.

### 2.2.2 Supervoxel cluster center identification

For each voxel  $p$ , find a neighboring voxel  $q$  in  $N(p)$  such that  $q$  has a higher density  $D(q) > D(p)$  in Eq. (4). Among voxels satisfying this condition, select the voxel  $q_c$  that is most similar to  $p$ , minimizing the similarity  $S(p, q)$ , Eq. (3). All voxels with the same  $q_c$  are members of the same supervoxel: it says that voxel  $p$  points to  $q_c$ . This process is repeated iteratively. Consider a voxel  $p$  that points to  $q_{c1}$ , where voxel  $q_{c1}$  points to another cluster center  $q_c$ . In this case  $p$  is now associated with the supervoxel centered on  $q_c$ . This assignment continues until there is no change in clustering. Voxels pointing to the same  $q_c$  form a supervoxel.

### 2.2.3 Gray-scale value replacement

Replace the gray-scale values of all voxels within the same supervoxel with that of the supervoxel center voxel  $I(q_c)$ .

### 2.2.4 Threshold segmentation

As shown later, this algorithm tends to aggregate the gray-scale values of the clusters into distinct peaks with few inter-

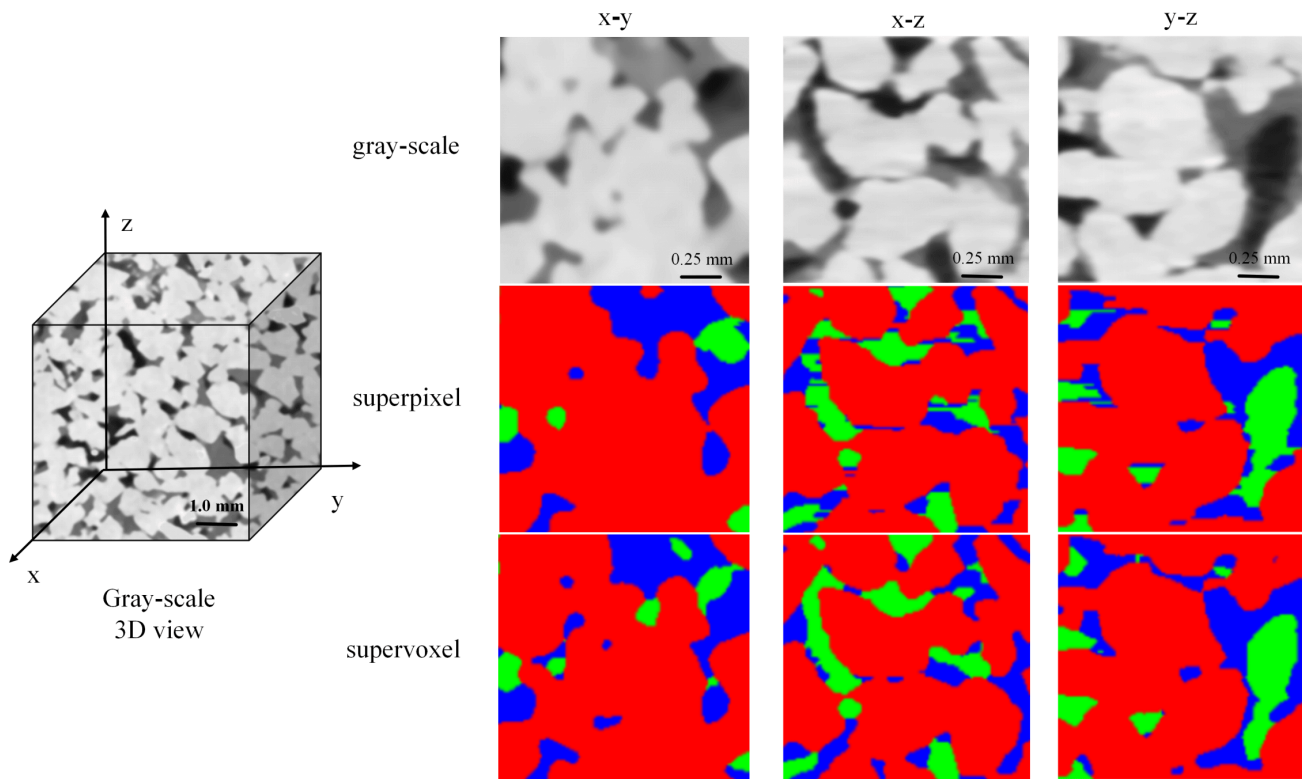


**Fig. 2.** Comparison of superpixel and supervoxel segmentation. (Top) Slices along different planes of three-dimensional Bentheimer sandstone raw X-ray images. (Middle) Segmentation results of the two-dimensional superpixel algorithm in the planes indicated. (Bottom) Segmentation results of the three-dimensional supervoxel algorithm.

mediate values. The image, after gray-scale value replacement, can be easily segmented by selecting an appropriate gray-scale threshold. This work set threshold values between two peak values in the histogram.

### 2.3 Contact angle and curvature measurements

The capillary pressure is equal to the average curvature of the fluid/fluid interface times the interfacial tension from the Young-Laplace equation (Bear, 2013). Commercial image analysis software, Avizo, was used to find the curvature. The *in situ* contact angles characterize the wettability of the system. This study applied an automated contact angle measurement algorithm to measure the distribution of contact angle along the three-phase contact loops (where the two fluid phases encounter the solid) identified from the segmented images (Alhammedi et al., 2017; Lin et al., 2019).

## 3. Results and discussion

### 3.1 Visual accuracy and efficiency

As shown in Fig. 4, the supervoxel algorithm segments the raw three-dimensional gray-scale image into distinct supervoxels based on voxel similarity, ensuring uniform gray-scale values within each supervoxel. This approach is advantageous, as evidenced by the gray-scale histogram: the most ambiguous voxels are those located between the peaks. After segmentation, the three peaks in the histogram become more distinct, significantly reducing ambiguity and enabling easier

segmentation through threshold selection.

The results demonstrate visually that the proposed supervoxel segmentation method outperforms the seeded watershed method which from previously published work (Lin et al., 2019), capturing more micro-porous structures and providing a more accurate representation of different liquid phases within the pore space.

Additionally, the algorithm is highly efficient and operates in an unsupervised manner, eliminating the need for segmentation labels prior to processing. This reduces the time spent on image annotation and model training compared to methods like Weka and neural networks. Furthermore, the algorithm can be parallelized across multiple CPU cores, resulting in very short run times.

### 3.2 Testing the segmentation model's generalizability

When using machine learning-based segmentation models, it is common for models to perform well on training data but struggle with new data, a phenomenon known as limited generalization or model transferability (Zhou et al., 2022). In contrast, our method requires no training data and generalizes easily to segment various porous media multiphase X-ray images. As shown in Fig. 5, we collected and segmented the eight 3D images listed previously to validate the robustness of our method: multiphase X-ray images of Bentheimer sandstone, a Middle Eastern reservoir carbonate, and Ketton limestone under both water-wet and mixed-wet conditions. Additionally,

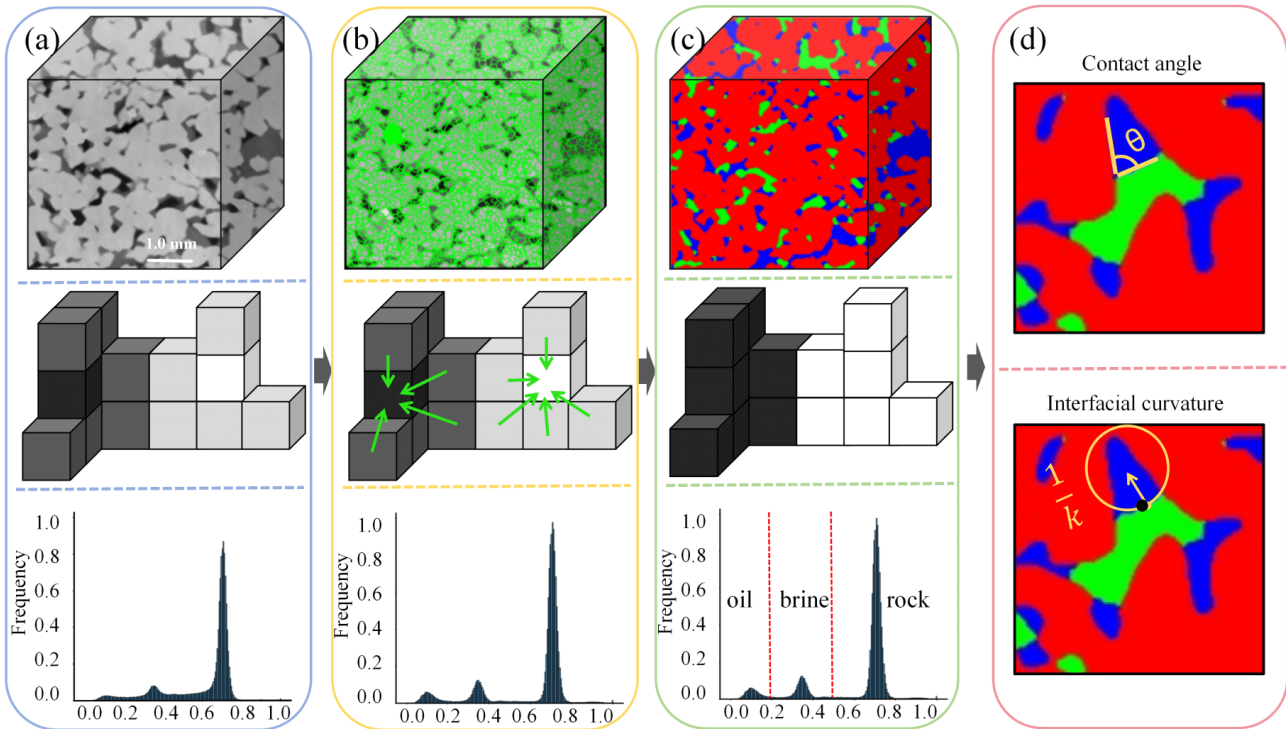


**Fig. 3.** The workflow for supervoxel segmentation and image analysis. (a) The distribution of gray-scale intensity in the image. The middle figure is a schematic showing individual voxels. The bottom figure is the gray-scale histogram of the top image. (b) Supervoxels are identified by clustering voxels that are most similar using Eq. (3) and associating a cluster center based on the density  $D(p)$  defined in Eq. (4). The green lines in the top figure shown the boundaries of supervoxel regions, while the arrows in the middle figure indicate which voxels are associated with the two supervoxel centers shown. (c) Gray-scale value replacement, where all voxels within a supervoxel adopt the gray-scale value of the cluster center  $I(q_c)$ . In the top figure this leads to a simple threshold-based segmentation of the image into three phases: grain (red), oil (green) and brine (blue). The bottom figure shows the selected thresholds from the gray-scale histogram of the image after clustering. (d) A schematic showing how contact angle and interfacial curvature are measured on the segmented image.

the algorithm effectively segments the gas diffusion layer containing air and water in the pore space. Despite the fibrous, elongated structure of the fibrous solid phase, which differs from typical rock formations, our algorithm performs well. These results indicate that the proposed supervoxel segmentation algorithm is highly versatile and suitable for the segmentation of most porous media multiphase X-ray images. Details on gray-scale histogram distribution of images used for validation before and after superpixel segmentation can be found in the Supplementary Information (Fig. S2). It is worth noting that the algorithm is not sensitive to image quality, even for the original image containing noise or low resolution image can still achieve effective segmentation. Different kinds and degrees of noise has been added to the images to further verify the anti-noise ability of the algorithm, as shown in Fig. 6.

### 3.3 Curvature and contact angle

Contact angles were calculated from a  $500 \times 500 \times 500$  voxel subvolume centered within the full images. As shown in Fig. 7(a), both segmentation methods produced similar contact angle distributions, with variances of less than  $20^\circ$ . For the water-wet and mixed-wet samples, the average contact angles

measured by the watershed and supervoxel methods were  $66.6^\circ$  and  $79.8^\circ$ , and  $69.9^\circ$  and  $77.3^\circ$ , respectively. Even in unfiltered mixed-wet samples, contact angle distributions and mean values were consistent with those of the filtered samples. As shown in Fig. 7(b), curvature measurements show predominantly positive values in the water-wet condition, as expected: the mode curvature values were  $0.0227$  and  $0.0226 \mu\text{m}^{-1}$  for the watershed and supervoxel methods, respectively. In the mixed-wet system, the mode curvature values were  $-0.0020$  and  $-0.0001 \mu\text{m}^{-1}$  for the watershed and supervoxel methods, respectively. Note that the magnitude of the curvature is at least one order of magnitude lower than in the water-wet system implying the presence of near minimal surfaces: the supervoxel algorithm implies that the mode curvature is almost exactly zero, consistent with the theoretical picture of interfaces in equilibrium pinned at boundaries between water-wet and oil-wet regions of the solid surface (Lin et al., 2019).

In analyzing additional properties as shown in Table 1, supervoxel segmentation yielded slightly higher porosity and a marginally lower Euler number (implying better connectivity) compared to watershed. Comparative analysis of the segmented images indicates that, relative to watershed segmentation, the supervoxel method captures smaller pores and

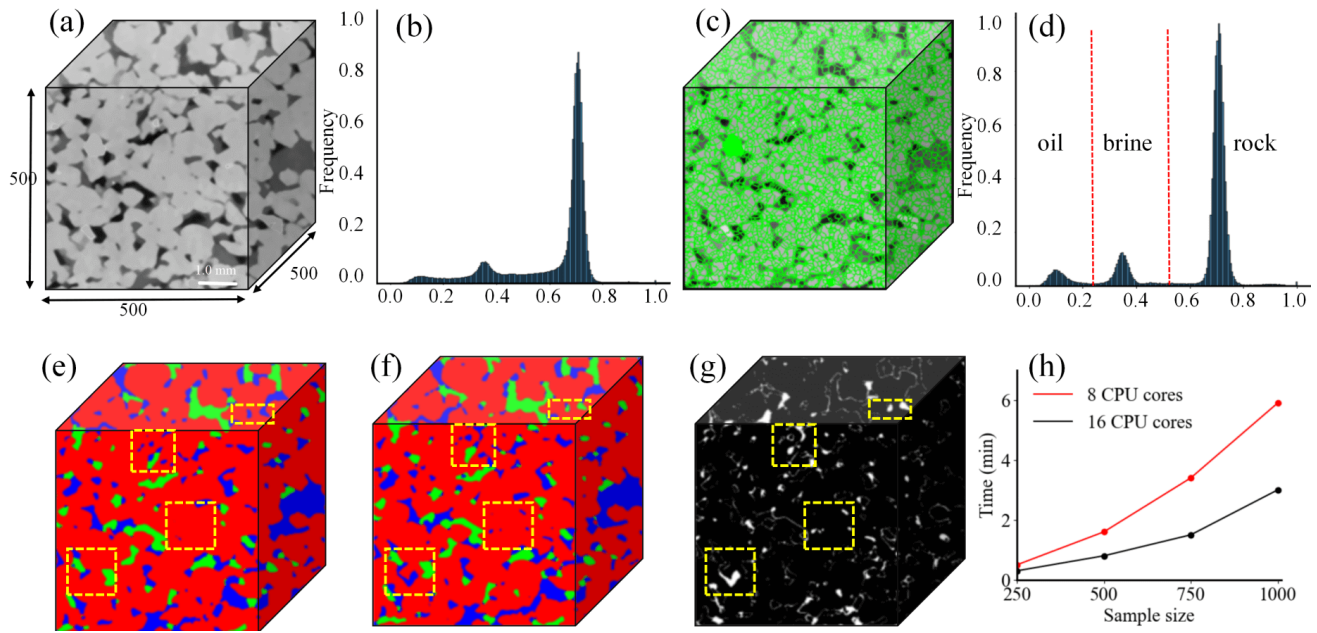


**Fig. 4.** Performance of supervoxel segmentation. (a) Gray-scale image of a Bentheimer sandstone sample under mixed-wet conditions, Fig. 1(b). (b) Histogram of the gray-scale values from (a). (c) Gray-scale image from (a) with supervoxels applied. (d) Histogram of the gray-scale values from (c). Segmented images showing rock (red), brine (blue), and oil (green) using the watershed algorithm (e), and the supervoxel algorithm (f). (g) Difference map between (e) and (f), with yellow boxes highlighting key differences between the two algorithms. (h) Computer time to segment images of different size using the supervoxel algorithm.

**Table 1.** Comparison of watershed and supervoxel methods under different experimental conditions.

Property	Watershed		Supervoxel		
	Mixed-wet	water-wet	Mixed-wet unfiltered	Mixed-wet	Water-wet
The average contact angle (°)	79.8	66.6	78.5	77.3	69.9
The standard deviation of contact angle (°)	18.0	16.1	18.5	19.2	16.1
The mode curvature values ( $\times 10^{-2} \mu\text{m}^{-1}$ )	-0.20	2.27	-0.05	-0.01	2.26
Porosity (%)	21.54	20.30	20.34	22.53	22.94
Saturation of water (%)	63.75	47.16	57.53	62.79	49.28
Saturation of oil (%)	36.25	52.84	42.47	37.21	50.72
Euler number of water	533	1745	942	48	-776
Euler number of rock	-2,853	-2,465	-3,290	-3,162	-5,620
Euler number of oil	696	331	803	775	266
Surface area of water ( $\times 10^6 \mu\text{m}^2$ )	5.8	6.3	6.1	6.5	6.6
Surface area of rock ( $\times 10^6 \mu\text{m}^2$ )	7.0	7.6	7.3	7.4	7.3
Surface area of oil ( $\times 10^6 \mu\text{m}^2$ )	3.2	3.9	3.8	3.6	3.2
Interfacial area of solid & oil ( $\times 10^6 \mu\text{m}^2$ )	3.6	3.5	4.3	3.8	4.0
Interfacial area of solid & water ( $\times 10^6 \mu\text{m}^2$ )	7.9	8.8	7.9	8.3	9.4
Interfacial area of oil & water ( $\times 10^6 \mu\text{m}^2$ )	1.8	1.4	2.4	2.3	1.3

Note: The 'mixed-wet unfiltered' segmentation image from watershed was omitted from analysis due to its absence in the referenced open-source dataset.

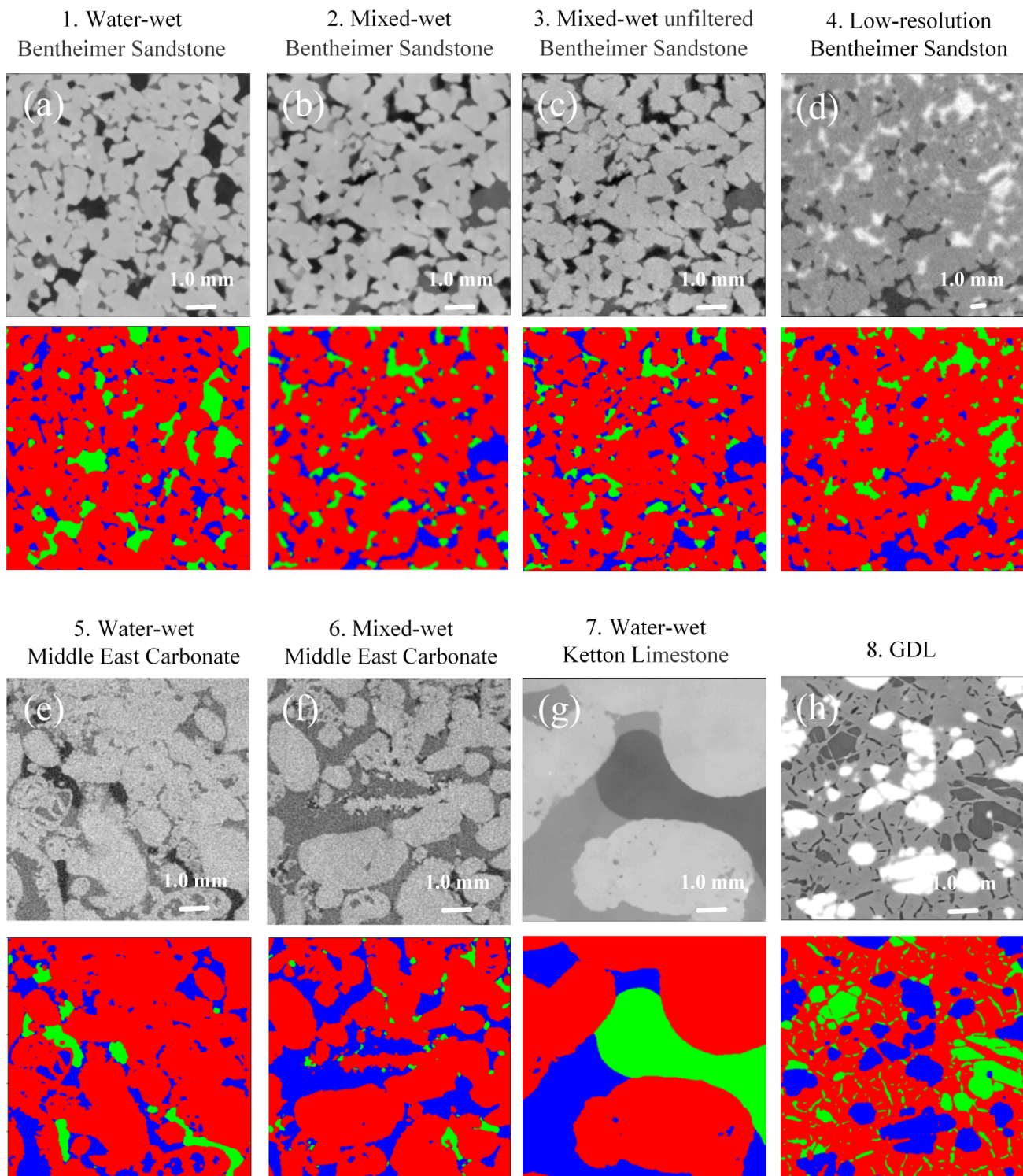


**Fig. 5.** Segmentation results of the supervoxel algorithm under various experimental conditions and for different porous media. (a-g) 2D slices from the 3D segmentation of different rock samples: rock (red), oil (green), and brine (blue) for images 1-7 in Fig. 1. (h) 2D slice from the 3D segmentation of a gas diffusion layer (GDL), image 8 in Fig. 1: fiber (red), air (green), and water (blue).

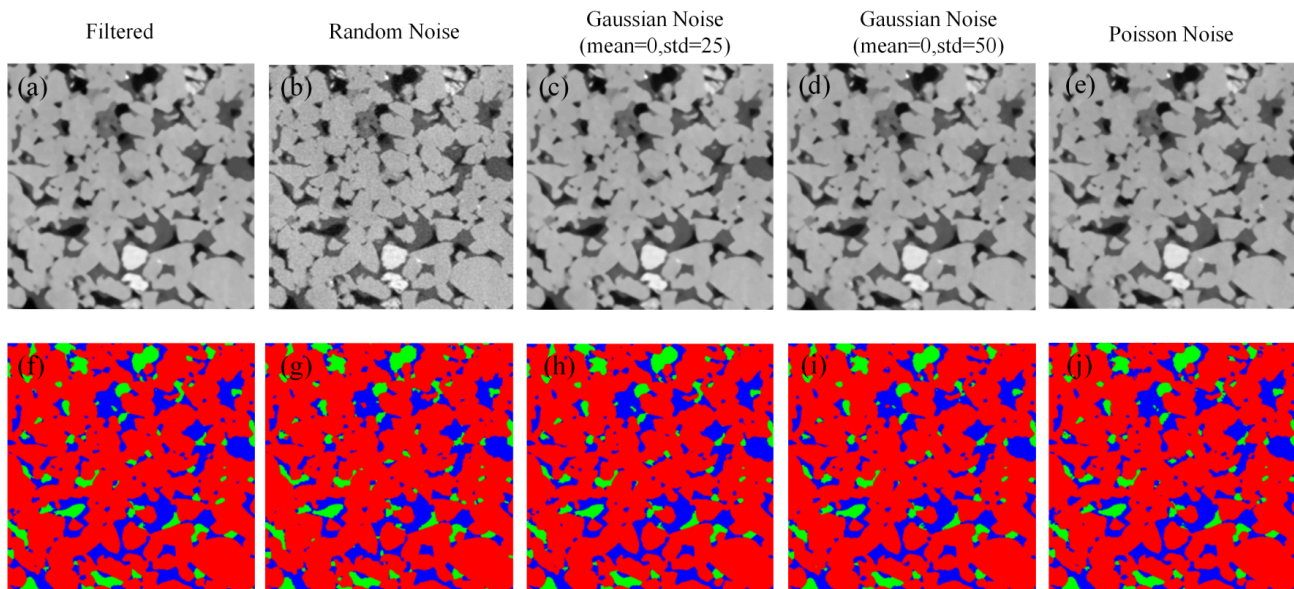


**Fig. 6.** The impact of different noise types on algorithm segmentation results. (a)-(e) respectively show filtered image (no noise added), unfiltered image with random noise, image with Gaussian noise (low standard deviation), image with Gaussian noise (high standard deviation), image with Poisson noise added; (f)-(j) present the segmentation results corresponding to (a)-(e).

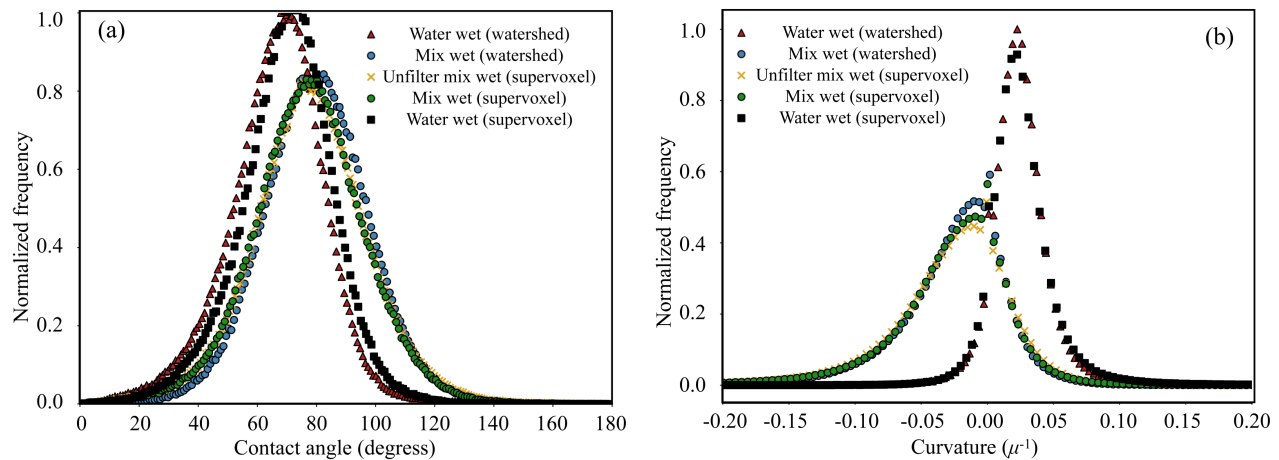


**Fig. 7.** Contact angle and curvature distributions for water-wet and mixed-wet Bentheimer sandstone with different segmentation methods: (a) The average contact angle of water-wet and the mixed-wet case the watershed and supervoxel methods, respectively and (b) The curvature values of water-wet and the mixed-wet case for the watershed and supervoxel methods, respectively.

provides improved connectivity between void spaces.

#### 4. Conclusions

This work has developed a supervoxel-based segmentation algorithm to segment X-ray micro-CT images of porous materials accurately and efficiently. Unlike traditional machine learning and deep learning methods, our approach is an unsupervised algorithm that requires no manual annotation, offering robust performance even in high-noise, low-resolution environments.

Validation on multiple datasets under varied experimental conditions demonstrates the algorithm's generalization and reliability, achieving precise segmentation for different materials. Additionally, the algorithm's parallel processing capabilities

enable rapid segmentation of large 3D images, drastically reducing computation time.

Overall, the proposed 3D supervoxel segmentation method effectively enhances the segmentation quality of X-ray micro-CT images of porous materials by preserving essential structural details and minimizing noise and redundancy. This makes it a reliable tool for analyzing diverse porous media in geophysics, material science, groundwater studies, and CO<sub>2</sub> storage.

#### Acknowledgements

The authors express their appreciation for the National Science Fund for Distinguished Young Scholars (No. 52125401). In addition, Shanlin Ye acknowledges the China Scholarship



Council for financial support during his visit to the imperial college london. The code of this work is available on GitHub: [GitHub Repository](#).

### Additional information: Author's email

xiaolizhi@cup.edu.cn (L. Xiao);  
g.wen@imperial.ac.uk (G. Wen);  
b.bijeljic@imperial.ac.uk (B. Bijeljic);  
m.blunt@imperial.ac.uk (M. J. Blunt).

### Supplementary file

<https://doi.org/10.46690/ager.2025.04.06>

### Conflict of interest

The authors declare no competing interest.

**Open Access** This article is distributed under the terms and conditions of the Creative Commons Attribution (CC BY-NC-ND) license, which permits unrestricted use, distribution, and reproduction in any medium, provided the original work is properly cited.

### References

- Achanta, R., Shaji, A., Smith, K., et al. Slic superpixels compared to state-of-the-art superpixel methods. *IEEE Transactions on Pattern Analysis and Machine Intelligence*, 2012, 34(11): 2274-2282.
- Alhammedi, A. M., AlRatrouf, A., Singh, K., et al. In situ characterization of mixed-wettability in a reservoir rock at subsurface conditions. *Scientific Reports*, 2017, 7(1): 10753.
- AlRatrouf, A., Raeini, A. Q., Bijeljic, B., et al. Automatic measurement of contact angle in pore-space images. *Advances in Water Resources*, 2017, 109: 158-169.
- Andrew, M., Bijeljic, B., Blunt, M. J. Pore-scale contact angle measurements at reservoir conditions using X-ray microtomography. *Advances in Water Resources*, 2014, 68: 24-31.
- Arganda-Carreras, I., Kaynig, V., Rueden, C., et al. Trainable weka segmentation: A machine learning tool for microscopy pixel classification. *Bioinformatics*, 2017, 33(15): 2424-2426.
- Blunt, M. J., Bijeljic, B., Dong, H., et al. Pore-scale imaging and modelling. *Advances in Water Resources*, 2013, 51: 197-216.
- Bear J. *Dynamics of Fluids in Porous Media*. New York, USA, Courier Corporation, 2013.
- Da Wang, Y., Shabaninejad, M., Armstrong, R. T., et al. Deep neural networks for improving physical accuracy of 2D and 3D multi-mineral segmentation of rock micro-CT images. *Applied Soft Computing*, 2021, 104: 107185.
- Garfi, G., John, C. M., Berg, S., et al. The sensitivity of estimates of multiphase fluid and solid properties of porous rocks to image processing. *Transport in Porous Media*, 2020, 131(3): 985-1005.
- Ibekwe, A., Pokrajac, D., Tanino, Y. Automated extraction of in situ contact angles from micro-computed tomography images of porous media. *Computers and Geosciences*, 2020, 137: 104425.
- Isah, A., Mahmoud, M., Aljawad, M. S., et al. Enforced CO<sub>2</sub> mineralization in anhydrite-rich rocks. *Energy*, 2024, 305: 132323.
- Kirillov, A., Mintun, E., Ravi, N., et al. Segment anything. Paper Presented at IEEE/CVF International Conference on Computer Vision, Faris, 4-6 October, 2023.
- Liang, J., Sun, Y., Lebedev, M., et al. Multi-mineral segmentation of micro-tomographic images using a convolutional neural network. *Computers and Geosciences*, 2022, 168: 105217.
- Lin, Q., Bijeljic, B., Berg, S., et al. Minimal surfaces in porous media: Pore-scale imaging of multiphase flow in an altered-wettability bentheimer sandstone. *Physical Review E*, 2019, 99(6): 063105.
- Lin, Q., Bijeljic, B., Pini, R., et al. Imaging and measurement of pore-scale interfacial curvature to determine capillary pressure simultaneously with relative permeability. *Water Resources Research*, 2018, 54(9): 7046-7060.
- Liu, H., Mao, L., Ju, Y., et al. Damage evolution in coal under different loading modes using advanced digital volume correlation based on X-ray computed tomography. *Energy*, 2023, 275: 127447.
- Li, X., Li, B., Liu, F., et al. Advances in the application of deep learning methods to digital rock technology. *Advances in Geo-Energy Research*, 2023, 8(1): 5-18.
- Mahdaviara, M., Sharifi, M., Rafiei, Y. Poreseg: An unsupervised and interactive-based framework for automatic segmentation of X-ray tomography of porous materials. *Advances in Water Resources*, 2023a, 178: 104495.
- Mahdaviara, M., Shojaei, M. J., Siavashi, J., et al. Deep learning for multiphase segmentation of X-ray images of gas diffusion layers. *Fuel*, 2023b, 345: 128180.
- Ramstad, T., Idowu, N., Nardi, C., et al. Relative permeability calculations from two-phase flow simulations directly on digital images of porous rocks. *Transport in Porous Media*, 2012, 94(2): 487-504.
- Reynolds, C. A., Menke, H., Andrew, M., et al. Dynamic fluid connectivity during steady-state multiphase flow in a sandstone. *Proceedings of the National Academy of Sciences*, 2017, 114(31): 8187-8192.
- Schlüter, S., Sheppard, A., Brown, K. Image processing of multiphase images obtained via X-ray microtomography: A review. *Water Resources Research*, 2014, 50(4): 3615-3639.
- Shojaei, M. J., Bijeljic, B., Zhang, Y., et al. Minimal surfaces in porous materials: X-ray image-based measurement of the contact angle and curvature in gas diffusion layers to design optimal performance of fuel cells. *ACS Applied Energy Materials*, 2022, 5(4): 4613-4621.
- Siavashi, J., Mahdaviara, M., Shojaei, M. J., et al. Segmentation of two-phase flow X-ray tomography images to determine contact angle using deep autoencoders. *Energy*, 2024, 288: 129698.
- Stutz, D., Hermans, A., Leibe, B. Superpixels: An evaluation of the state-of-the-art. *Computer Vision and Image Understanding*, 2018, 166: 1-27.
- Vedaldi, A., Soatto, S. Quick shift and kernel methods for mode seeking. Presented at 10<sup>th</sup> European Conference

- on Computer Vision, Marseille, France, 12-18 October, 2008.
- Vincent, L., Soille, P. Watersheds in digital spaces: An efficient algorithm based on immersion simulations. *IEEE Transactions on Pattern Analysis and Machine Intelligence*, 1991, 13(6): 583-598.
- Wildenschild, D., Sheppard, A. P. X-ray imaging and analysis techniques for quantifying pore-scale structure and processes in subsurface porous medium systems. *Advances in Water Resources*, 2013, 51: 217-246.
- Yang, Y., Horne, R. N., Cai, J., et al. Recent advances on fluid flow in porous media using digital core analysis technology. *Advances in Geo-Energy Research*, 2023, 9(2): 71-75.
- Yang, J., Zhou, Y. An automatic in situ contact angle determination based on level set method. *Water Resources Research*, 2020, 56(7): e2020WR027107.
- Yang, Y., Zhou, Y., Cai, J., et al. Advances in multiscale numerical and experimental approaches for multiphysics problems in porous media. *Advances in Geo-Energy Research*, 2021, 5(3): 233-238.
- Zeng, F., Dong, C., Lin, C., et al. Pore structure characteristics of reservoirs of xihu sag in east china sea shelf basin based on dual resolution X-ray computed tomography and their influence on permeability. *Energy*, 2022, 239: 122386.
- Zhao, Z., Lu, H. Deep learning interprets failure process of coal reservoir during CO<sub>2</sub>-desorption by 3D reconstruction techniques. *Energy*, 2023, 282: 128802.
- Zhou, K., Liu, Z., Qiao, Y., et al. Domain generalization: A survey. *IEEE Transactions on Pattern Analysis and Machine Intelligence*, 2022, 45(4): 4396-4415.
- Zhu, L., Ma, Y., Cai, J., et al. Key factors of marine shale conductivity in southern China-Part II: The influence of pore system and the development direction of shale gas saturation models. *Journal of Petroleum Science and Engineering*, 2022, 209, 109516.
- Zhu, L., Bijeljic, B., Blunt, M. J. Generation of pore-space images using improved pyramid Wasserstein generative adversarial networks. *Advances in Water Resources*, 2024, 190, 104748.